



Transparent conductors for Mid-infrared liquid crystal spatial light modulators

Fabian G. Micallef^a, Pawan K. Shrestha^a, Daping Chu^{a*}, Kenneth McEwan^b, Girish Rughoobur^c, Tian Carey^d, Nigel Coburn^c, Felice Torrisi^d, Oihana Txoperena^e, Amaia Zurutuza^e

^a Centre for Photonic Devices and Sensors, Department of Engineering, University of Cambridge, 9 JJ Thomson Ave, Cambridge, United Kingdom

^b Defence Science and Technology Laboratory (DSTL), Salisbury, United Kingdom

^c Solid State Electronics and Nanoscale Science, CAPE, Department of Engineering, University of Cambridge, 9 JJ Thomson Ave, Cambridge, United Kingdom

^d Cambridge Graphene Centre, University of Cambridge, 9 JJ Thomson Ave, CB3 OFA Cambridge, United Kingdom

^e Graphenea, Paseo Mikeletegi 83, San Sebastián 20009, Spain

ARTICLE INFO

Keywords:

Mid-infrared
Transparent conductors
Ultra-thin metallic films
Nickel
Copper
CVD graphene
Nematic liquid crystals
Spatial light modulation

ABSTRACT

Transparent conductors (TCs) are required for liquid crystal spatial light modulators (LC-SLMs) in order to set up an electric field across the LC layer. In the middle infrared (Mid-IR) range ($\lambda = 2$ to $5 \mu\text{m}$), LC-SLMs can offer a low-cost, non-mechanical, random-access and compact alternative to the gimballed mirrors used currently for Mid-IR laser beam-steering. Indium tin oxide (ITO) is the industry standard for applications in the visible spectrum but it performs poorly in the IR, with a transmittance $< 20\%$ for Mid-IR wavelengths. Little work has been done to develop a comparable material which fulfills the required properties in the Mid-IR: A sheet resistance allowing operation at typical frequencies ($\approx 1 \text{ kHz}$) and, if patterned, with minimal voltage drop along the electrode, a transmittance $> 50\%$ in the target range, chemical, thermal and mechanical robustness which can endure subsequent processing, and ability to be patterned at low-cost to a resolution comparable to the wavelengths investigated. Ni and Cu ultra thin metallic films (UTMFs), Cu_xO thin films (TFs), and chemical vapour deposition (CVD) grown mono-layer graphene were investigated. Ni UTMFs and graphene were found to have the best performance with sheet resistance values of $747 \pm 86 \Omega/\square$ and $360 \pm 34 \Omega/\square$ respectively for samples having a transmittance of 65% and 97% at $\lambda = 2.3 \mu\text{m}$. Both Ni UTMFs and CVD mono-layer graphene were found to be suitably stable with age. An increase of sheet resistance after baking was recorded due to oxidation and desorption of contaminating dopants respectively. Ni UTMFs were found to be patternable down to a $3 \mu\text{m}$ resolution, limited by the mask, using a standard photo-lithographic lift-off process. Transmissive LC cells with a maximum phase shift of 3π at $\lambda = 2.3 \mu\text{m}$ were assembled with both Ni UTMFs and mono-layer graphene as TCs on sapphire, with the former having transmittance of 18.7% and contrast ratio of 25.0, and the latter having transmittance of 81.1% and contrast ratio of 50.7.

1. Introduction

Liquid crystal spatial light modulators (LC-SLMs) have a broad range of applications from displays [1] to aberration control and beam-steering [2]. Liquid crystal (LC) materials have strong non-linear optical properties in the visible and IR spectra, however absorption peaks in the IR can limit their use [3]. Additionally, their flexibility of implementation has enabled their use for many applications [4]. For example, the liquid crystal display (LCD) industry has accelerated material and device research greatly and driven down the cost of production considerably [5].

Adaptation of LC-SLM technology to the middle infrared (Mid-IR)

frequency range holds great promise for a number of important applications. In communications, pushing up the carrier frequency results in a more focused beam, which increases the efficiency. A higher carrier frequency also increases the bandwidth [6]. Sensing in the Mid-IR offers many possibilities since transmissive atmospheric bands in the Mid-IR [7] allow for laser radar systems with greater resolution than microwave or radio systems. This opens up a range of mostly, but not limited to, security and military oriented applications. Infrared (IR) countermeasure systems [8] along with targeting and navigation systems are of great interest. Other, more civilian-oriented, applications are precise fire detection and laser RADAR systems for the automotive industry and terrain mapping of IR emitting sources of geological,

* Corresponding author.

E-mail address: dpc31@cam.ac.uk (D. Chu).

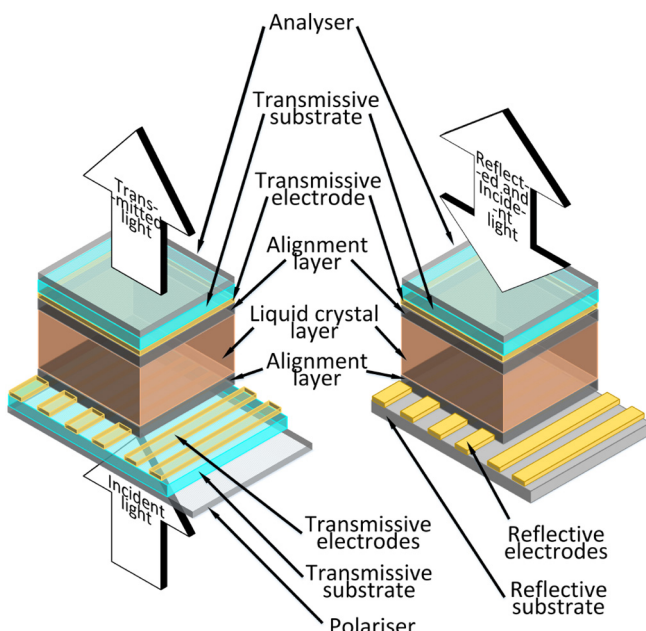


Fig. 1. Cross-section of a transmissive and reflective LC SLM respectively [14].

biological or environmental importance [5,9,10].

As such, LC-SLM devices have great potential in being a cost effective, compact and reliable alternative to the current state-of-the-art, such as gimbaled mirrors [11]. In addition to being completely non-mechanical, LC devices are entirely random access, since to address two independent angles there is no need to go through all the angles in between, and has negligible inertia considerations [12]. For a fully addressable pixel structure, multiple functionalities (fanout, lensing, aberration compensation) can be implemented without any additional cost or device complexity [13].

A basic LC-SLM device is formed of five essential components as shown in Fig. 1. Firstly, there is the liquid crystal layer which provides the variable retardation necessary to set up the optical delay patterns. This layer is enclosed between two substrates where either one or both, for reflective and transmissive devices respectively, must be transmissive in the operational frequency. Patterned electrodes on these substrates set up the electric field necessary to reorient the LC molecules, thus varying the refractive index and therefore the phase retardation. They are also reflective or transmissive depending on the setup. Alignment layers in contact with the LC-layer lock the orientation of the liquid crystal molecules at the boundaries and therefore determine the behaviour of the LC-SLM in the off-state. LC-SLM operation depends on the polarisation of the incident light. Therefore, unless the source light is already polarised a polariser is used. An analysing polariser on top of the device is used to obtain light and dark states for amplitude modulating devices and as a way to visualise phase changes in the development of phase modulating devices [14].

In developing such a device for Mid-IR operation two material challenges stand out: Finding a transparent conductor (TC) which is transmissive in the desired wavelength range and an LC-material which is both transmissive and retains good optical anisotropy in the same range. Particular to this work are the challenges with regards to the transparent conductor: A sheet resistance which allows LC-SLM operation at typical frequencies (≈ 1 kHz) and, if patterned, with minimal voltage drop along the electrode, a transmittance of at least 50% in the target range, chemical, thermal and mechanical robustness which can endure subsequent processing steps, and ability to be patterned at low-cost to a resolution comparable to the wavelengths investigated. Indium tin oxide (ITO) is the industry standard for applications in the visible spectrum but it performs poorly in the IR, with a transmittance $< 20\%$

for Mid-IR wavelengths [15]. A viable alternative has to be found if further progress is to be made.

2. Sample preparation and experimental setup

Cu, Ni and Cu_xO film samples were prepared in a DC magnetron sputtering system (Metallifier Sputter Coater, Precision Atomics, Cambridge, UK). The sputtering targets used were high purity (99.9% purity) 4 inch diameter by 3 mm thick targets. Sputtering power was fixed at 100 W and the process pressure was set to 350 Pa. Graphene was grown by chemical vapour deposition (CVD) (Graphenea) on a copper foil at 1000 °C. A PMMA layer was spin-coated onto the graphene surface as a sacrificial layer. Graphene was detached from the Cu foil by wet etching of the Cu foil using a solution of FeCl_3 , and subsequent cleaning steps were done in de-ionized water. Next, the graphene layer with the PMMA was transferred onto the final substrate and dried on a hot plate to remove the excess of water. Last, the PMMA layer was removed with acetone. Samples were deposited on soda lime glass (1.1 mm) for investigating sheet resistance and the effects of heating and ageing on the samples. Sapphire substrates (0.3 mm) were used for optical tests, due to its superior transmittance up to 5 μm , and etching tests.

An EVG620 Automated Mask Alignment System was used for photolithography in the patterning process. Due to the nm scale thicknesses involved a lift-off process with Microposit S1818 was used. Pre-baking and baking steps were conducted in an oven instead of a hotplate due to the thermally insulating nature of the substrates used. Baking time was slightly increased to account for heat loss in opening and closing of the oven. After the conducting material was sputtered upon the patterned photo-resist, lift-off was conducted using acetone in an ultrasonic bath.

Sheet resistance R_{\square} was measured using a Jandel probe head in a 4-point probe configuration. transmittance data was collected for the wavelength range 1.6–6.5 μm using a Cary 600 Series FTIR spectrometer. Film thickness and composition was probed using both spectroscopic ellipsometry (Horiba Jobin Yvon UVISEL Spectroscopic Ellipsometer) and atomic force microscopy (AFM) (Agilent 5420 AFM/SPM).

For ageing, samples were stored in a sealed container at atmospheric pressure in a room-temperature, low-humidity environment and R_{\square} values were collected at intervals. For baking, samples were heated on a hotplate, at different temperatures and at atmospheric pressure, in a room-temperature, low-humidity environment so that R_{\square} data could be collected efficiently.

Single pixel LC cells were assembled using both Ni UTMF and graphene mono-layer on sapphire substrates. Ni UTMF samples were spin coated with nylon in formic acid (2:998) at 3000 rpm for 30 s. Ni UTMF Samples were then baked at 200 °C for 120 min. All samples were rubbed using a rubbing machine for the LC alignment. These rubbed layers were glued in an anti-parallel configuration facing each other with 15 μm spacers in between to form the cell. The cell gap of the empty cell was measured to be $15 \pm 0.7 \mu\text{m}$ across the device using spectral interference fringes. The cell was then filled with NLC BL037 at 110 °C using capillary effect followed by slowly cooling down to room temperature. The filling hole of the cell was sealed and wires were bonded using silver epoxy to form an electrical connection. Multiple working LC SLMs were fabricated to confirm the reproducibility of the process.

The LC SLMs' electro-optic response was observed between crossed polarisers at $\lambda = 2.3 \mu\text{m}$. A $\text{Cr}^{2+}:\text{ZnS}/\text{Se}$ Laser (IPG Photonics) was used as a laser light source. An InGaAs Detector (Thorlabs) was used for data collection.

Table 1

Thickness and composition data obtained from measured reflective ellipsometry data. t_{est} is the estimated thickness from standard sputtering recipes, t_m is the thickness of the metal/void effective medium layer, $\%m$ is the percentage of metal in the metal/void effective medium layer, t_{ox} is the thickness of oxide at the air/film interface, t_{tot} is the total thickness if an effective medium model having metal/oxide/void is used, $\%ox$ is the percentage of oxide if an effective medium model having metal/oxide/void is used and χ^2 is a measure of the goodness of the fit.

	t_{est} (nm)	t_m (nm)	$\%m$	t_{ox} (nm)	χ^2
Ni UTMF	6	11.17 ± 1.18	81.0 ± 5.08	0.02 ± 0.03	1.30
	3	5.99 ± 1.47	58.7 ± 5.2	0.05 ± 0.12	0.80
Cu UTMF	9	13.77 ± 2.15	78.9 ± 5.3	0.69 ± 0.22	0.16
	6	8.84 ± 1.45	68.0 ± 4.9	1.77 ± 0.09	0.35
t_{tot} (nm)		$\%ox$			
Cu_xO TF	4	3.20 ± 0.65	12.7 ± 4.5	70.5 ± 5.4	3.46
	10	18.20 ± 0.36	55.1 ± 1.6	24.3 ± 3.3	0.84
	5	10.99 ± 1.22	45.5 ± 1.6	1.2 ± 14.5	0.08

3. Results and discussion

3.1. Film morphology

Typical thickness and composition values for freshly deposited samples collected by reflective ellipsometry are given in Table 1. The empirical model used to obtain the above is formed by four layers for UTMFs in the order air, oxide, metal/void, substrate. This agrees with literature for a copper or nickel granular film that is exposed to air since a layer of Cu_2O or NiO respectively forms at the air/metal interface [16,17]. All layers are assumed to be homogeneous and isotropic, with a Bruggeman effective medium model [18] used to explain the metal/void layer. For Ni and Cu UTMFs the data shows good fitting with the model. For Cu_xO TFs this model is not appropriate since we do not expect the oxide layer to be separate from the metal/void layer. In this case the Bruggeman effective medium model combined Cu, Cu_2O and voids even though a higher concentration of Cu_2O is still expected at the air/film interface. Due to the large oxidation in air the same treatment as Cu_xO TFs was used for 4 nm Cu films. As the Cu_xO films tested were deposited with a low oxygen to argon flow ratio of 3:28, this resulted in films that were a particulate composite of primarily metallic Cu and Cu_2O along with voids, as seen in literature [19].

The estimated sputter thickness, t_{est} , in Table 1 was obtained by assuming proportionality between sputtering time and film thickness so that standard lab recipes, which are designed for micron-scale films, could be used. From the model fit to the ellipsometry data for UTMFs t_m is the metal/void thickness, $\%m$ is percentage of metal in the metal/void layer and t_{ox} is the oxide thickness. For Cu_xO thin films (TFs) t_{tot} is the total thickness while $\%m$ and $\%ox$ are the percentage of Cu and Cu_2O in the layer respectively.

Properties of nm-scale films depend highly on the granularity of the deposited material. Granularity is given by the size and shape of the grains that form the film. For a crystalline material a grain is a crystallite in a polycrystalline film. In general, a grain is a volume of the film which is separate from the rest by a boundary [20]. The size and shape of granules depends on the material deposited but also on the sputtering parameters, primarily oxygen partial pressure, if any, and sputtering power [19,21]. Fig. 2 shows the grains in 0.5 μm × 0.5 μm topographic AFM images for Ni UTMFs 3 nm and 6 nm, Cu UTMFs 6 nm and 9 nm and Cu_xO 5 nm.

Granule property data was obtained using the watershed method in Gwyddion software [22] and is summarised in Table 2, where t_{est} is the estimated sputter thickness, h_{gr} is the mean grain height with respect to the surrounding local minimum, obtained by subtracting the grain base height from the grain peak height, r_{gr-eq} is the equivalent grain radius for a perfectly circular grain of the same area as the detected grain

while $r_{gr-insc}$ is the radius of the largest circle which can be inscribed in the detected grain. Comparing the latter two parameters gives an estimate of the circularity of the grains, since an inscribed circle only has the same area as the equivalent circle if the grain is circular. Note also that h_{gr} is not a measure of the thickness of the film, but is effectively a “roughness” measurement localised to each grain. It can be seen that Ni UTMFs tend to form the largest granules for a given thickness, but at 6 nm the topography is considerably more even since h_{gr} is less than half that of 3 nm films, with a few large granules still dominating. This suggests that the spaces between the granules are being filled up. For films deposited using the same deposition parameters grain size is known to be linearly proportional to t_{est}^β for some factor β [23], and therefore the reduction in r_{gr-eq} and $r_{gr-insc}$ for increasing Ni UTMF thickness does not indicate that there is a reduction in grain size. From Fig. 2 particularly large granules do not appear for Cu and there is an increase in grain size which obeys the proportionality we expect. It is important to note that for Cu_xO TFs the central “V” shaped artefact that can be seen in Fig. 2 has been excluded from the analysis.

To successfully model the electrical and optical properties of our samples it is necessary to estimate the thickness and grain size of the thin films accurately. The estimated thickness values were obtained by dividing the sputtering time required to deposit known thicknesses, typically of a few μm . However our data shows that this proportionality does not hold. The model $t \propto t_{est}$, while appropriate for larger thicknesses, was changed to $t = A \times t_{est}^\alpha$, where A and α are proportionality constants, for our small thickness range [23]. Note that the oxide layer was not modelled as it has a negligible effect on the conductivity of the films due to its very high resistivity and its thickness does not have bearing on the transmissive properties at the wavelengths investigated due to the very low value of the extinction coefficient k [24,25]. Due to the proportionality relationship between thickness and grain size [23], the same model was used for grain size with B and β as proportionality constants. For Ni UTMFs and Cu_xO TFs the lack of AFM data for multiple thickness values meant that the β constant was the same as that for the thickness model α . This is justified by the fact that AFM data for Cu yields very close values of α for thickness and β for grain size. The void fraction ϕ , which comes into play for both the electrical and optical properties, was modelled using a model $\phi = Ce^{-\gamma t_{est}}$, where C and γ are proportionality constants, based on the ellipsometry data collected. These constants are given in Table 3.

It should be noted that modelling in Table 3 is for sputtered thin films. Graphene was not sputtered, hence could not be modelled in the same way. However, significant work has already been undertaken to estimate the thickness, grain size and number of defects in such graphene materials, such as the thickness of each atomic layer of graphene being 0.33 nm [26] and the changes of the grain size and defects (and thus the void percentage) as a function of the CVD growth conditions [27].

3.2. Electrical properties

Measured R_\square data for Cu, Ni and Cu_xO samples are illustrated in Fig. 3. The fitted data using the model described below are also presented in Fig. 3. Cu_xO TFs were found to have a sheet resistance up to 8 times larger than Ni and Cu UTMFs for equal thicknesses. It can also be observed that the sheet resistance for Cu UTMFs becomes larger than Ni UTMFs for thicknesses smaller than ≈ 10 nm, with the R_\square value for Cu UTMFs becoming more than twice as large as that for Ni UTMFs around 5 nm. CVD mono-layer graphene was found to have a sheet resistance of $360 \pm 34 \Omega/\square$ by taking readings from three different samples. This is comparable to Ni and Cu UTMFs between 7 nm and 9 nm thick. Note that for graphene, doping might occur during further processing stages, primarily due to the polyimide coating necessary for LC-SLM construction. This can potentially decrease the sheet resistance of the graphene layer considerably [28].

To explain the physical properties giving rise to such different

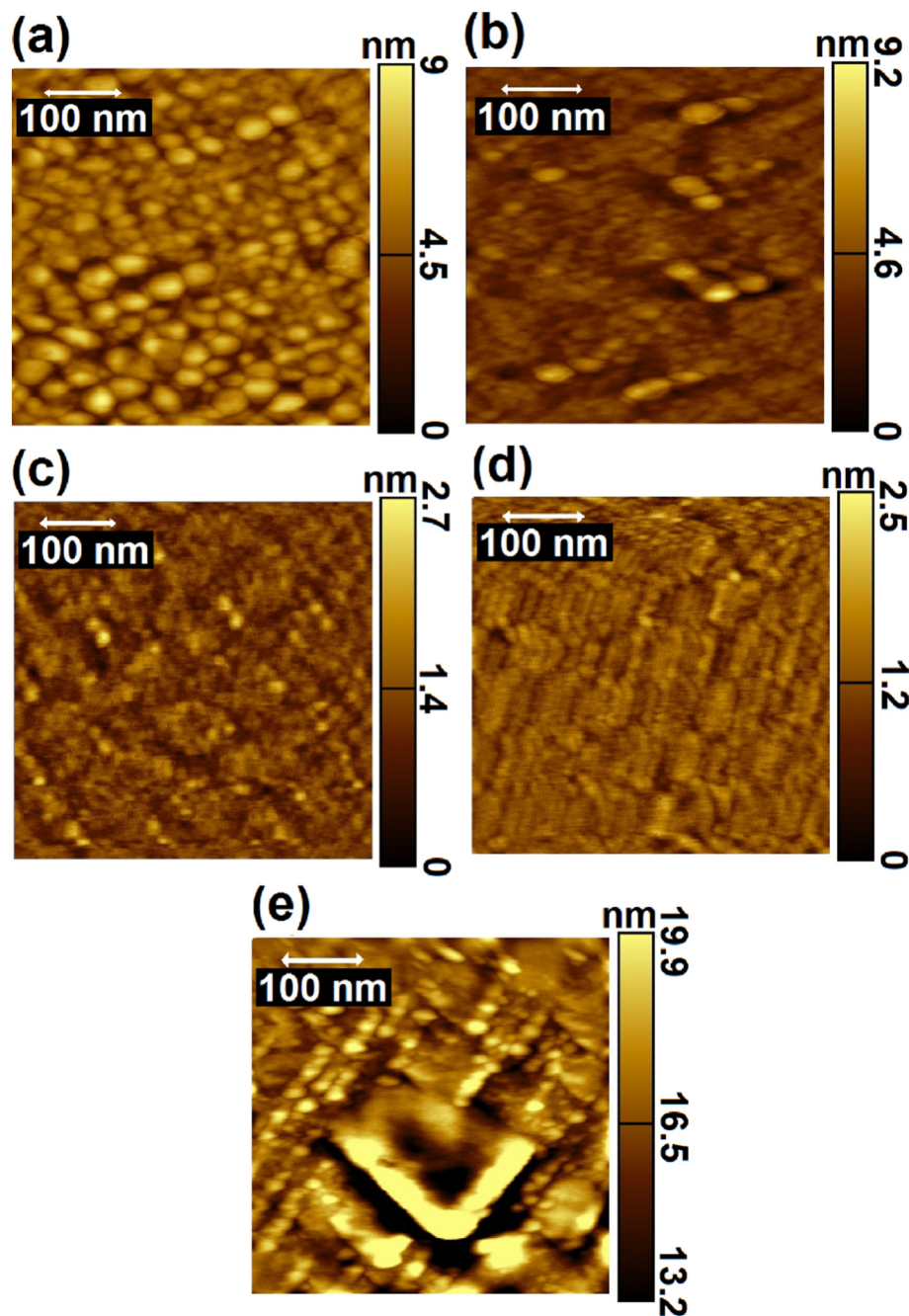


Fig. 2. $0.5 \mu\text{m} \times 0.5 \mu\text{m}$ topographic AFM images for deposited films: Ni UTMFs (a) 3 nm and (b) 6 nm, Cu UTMFs (c) 6 nm and (d) 9 nm and Cu_xO TFs (e) 5 nm.

Table 2

Granularity data obtained from the AFM images in Fig. 2 using the watershed method in Gwyddion software. t_{est} is the estimated thickness from standard sputtering recipes, h_{gr} is the mean grain height with respect to the surrounding local minimum, r_{gr-eq} is the equivalent grain radius for a circular grain of the same area and $r_{gr-insc}$ is the radius of the largest inscribed circle in the grain.

	t_{est} (nm)	h_{gr} (nm)	r_{gr-eq} (nm)	$r_{gr-insc}$ (nm)
Ni UTMF	3	1.33 ± 0.53	8.71 ± 3.57	5.22 ± 2.15
	6	0.48 ± 0.38	6.89 ± 4.94	3.13 ± 1.65
Cu UTMF	6	0.42 ± 0.13	5.00 ± 1.94	2.69 ± 0.99
	9	0.63 ± 0.14	10.93 ± 4.89	4.17 ± 1.01
Cu_xO TF	5	1.10 ± 0.52	5.44 ± 2.23	2.79 ± 1.11

Table 3

Model constants for thickness, grain size and void fraction. Thickness = $A \times t_{\text{est}}^\alpha$, grain size = $B \times t_{\text{est}}^\beta$ and void fraction = $C e^{-\gamma t_{\text{est}}}$.

	Thickness		Grain size		Void fraction	
	A	α	B	β	C	γ
Ni UTMF	2.153	0.919	3.805	0.919	0.899	$(\ln(2.175))/3$
Cu UTMF	1.264	1.085	0.775	1.081	4.067	0.391
Cu_xO TF	3.406	0.728	1.668	0.728	0.661	$(\ln(1.213))/5$

behaviour for different materials a model based on the combination of the Fuchs's theory (FS-model) [20] and the model by Mayadas and Shatzkes (MS-model) [20] were employed. The FS-model explains the increase in resistivity from the bulk resistivity value ρ_{bulk} for thin films by introducing a parameter p taking value from 0 to 1 with 0 implying

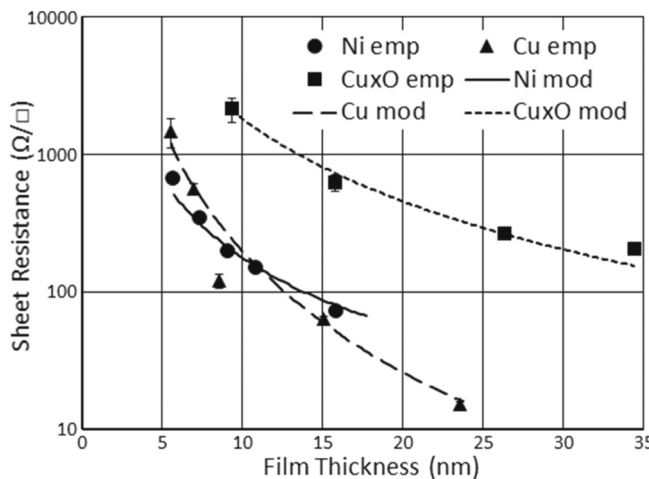


Fig. 3. Comparison of R_{\square} empirical data along with model fit for Ni and Cu UTMFs and Cu_xO TFs against film thickness.

complete diffuse electron reflection from the film surfaces and 1 implying complete specular electron reflection from the film boundaries. The MS-model considers the grain reflection coefficient R , again taking value between 0 and 1, to model the electron reflection that occurs at the boundaries between grains [20]. Note that the values of ρ_{bulk} taken for Ni and Cu were $69.9 \Omega \text{ nm}$ and $16.8 \Omega \text{ nm}$ respectively [29]. The FS-model is appropriate for thicker films but starts to underestimate the resistivity for smaller thicknesses, with 30 nm for Ni being the typical deviation point between empirical data and the FS-model [30]. For UTMFs, the effect of both models on ρ_{bulk} can be summated according to Mattheissen's Rule as higher order interactions between the two only come into play at temperatures far lower than the operational temperatures [30]. Therefore, for a resultant resistivity ρ we have

$$\rho = \rho_{bulk} + \Delta\rho_{FS} + \Delta\rho_{MS} \quad (1)$$

where $\Delta\rho_{FS} = \rho_{FS} - \rho_{bulk}$ and $\Delta\rho_{MS} = \rho_{MS} - \rho_{bulk}$

where ρ_{FS} and ρ_{MS} are the resistivities found by applying the FS and MS models respectively, which are given by [20]

$$\rho_{FS} = \rho_{bulk} \left[1 - \left(\frac{3}{2K} \right) (1-p) \int_1^{\infty} \left(\frac{1}{t^3} - \frac{1}{t^5} \right) \frac{1-e^{-Kt}}{1-pe^{-Kt}} dt \right]^{-1} \quad (2)$$

$$\rho_{MS} = \rho_{bulk} \left[1 - \frac{3\alpha}{2} + 3\alpha^2 - 3\alpha^3 \ln \left(1 + \frac{1}{\alpha} \right) \right]^{-1} \quad (3)$$

where $K = t_f/l$, where l is the electron mean free path and t_f is the film thickness, and $\alpha = (l/g)(R/(1-R))$, where g is the grain size. Note that the values of l taken for bulk nickel and copper were 5.87 nm and 39.9 nm respectively [29].

A further complication arises from the voids which form a considerable percentage of the volume of the deposited films. This means that the value of ρ_{bulk} found from data-sheets cannot be used. The Bruggeman model was used to obtain a corrected value for ρ_{bulk} [18]. This model assumes that inclusions, in this case voids, exist within a uniform matrix, in this case the metal, and that these inclusions do not interact. The behaviour of the model depends on two parameters: λ , the ratio of the conductivity of the inclusions with the conductivity of the matrix, and ϕ , the fraction by volume of inclusions as already described earlier, which takes a value between 0 and 1. In our case, where λ approaches 0 and taking ϕ values from the composition data collected by reflective ellipsometry, we have an expression for the corrected bulk resistivity, ρ'_{bulk} given by [18]

$$\rho'_{bulk} = \frac{\rho_{bulk}}{1 - \phi^{3/2}} \quad (4)$$

This change in the bulk resistivity creates a corresponding change in the electron mean free path l since the two are related by [20]

$$\rho'_{bulk} l' = \frac{12\pi^3 \hbar}{e^2 S_f} \quad (5)$$

where S_f is the free area of the Fermi surface, e is the charge of an electron and \hbar is the reduced Planck constant. S_f is introduced by a simplification, for polycrystalline films, of the general expression for the conductivity tensor [31], which involves an integral over the Fermi surface. The Fermi surface is known to change as the composition of the film changes [32]. We can therefore expect S_f to change too. It is however very difficult to model this change for our complex material and as such this value was extracted from the above for the bulk values ρ_{bulk} and l for each material and is kept constant throughout our investigation.

It is evident from literature that the R parameter increases dramatically for thicknesses less than 20 nm for a range of metals [23]. It is also clear that the p parameter becomes progressively less important as thickness drops to this range [23] where it can be set to 0 with confidence [20]. In this case, the R values fit to the data were $R = 0.981$ for Ni UTMFs, $R = 1 - 0.0105t_{est}$ for Cu UTMFs, giving $R = 0.97$ and $R = 0.84$ at t_{est} 4 nm and 15 nm respectively and $R = 0.99$ for all Cu_xO TFs.

Using the above model the relationship between the ρ values for Ni and Cu UTMFs and Cu_xO TFs can be interpreted in terms of the interplay between grain size and corrected bulk resistivity ρ'_{bulk} . These two values for our samples are shown in Fig. 4. In fact ρ'_{bulk} for Cu starts to increase dramatically at around 10 nm, while the grain size for Ni is larger throughout. Over 10 nm and throughout Cu_xO has dramatically larger ρ'_{bulk} than Cu, as expected.

3.3. Optical properties

Fig. 5 shows the transmittance (%) vs. λ (μm) for samples with selected values of t_{est} (nm). Samples tested are Ni and Cu UTMFs, Cu_xO TFs and CVD graphene mono-layer. In all cases the results include the effect of the sapphire substrate since this will be an integral part of any future work, and comparisons between the different materials can still be drawn with confidence as identical sapphire substrates were used for all tests. Graphene can be seen to have transmissive properties far better than any of the other samples, with a transmittance better than 97% across the whole range investigated once substrate effects are subtracted. In all other cases the performance is seen to decrease with increasing wavelength, even when accounting for the effects of the sapphire substrate, which only drops in transmittance sharply after 5 μm . Cu UTMFs have the largest transmittance, particularly for smaller values of t_{est} . Ni UTMFs follow, differing by approximately 15% at small

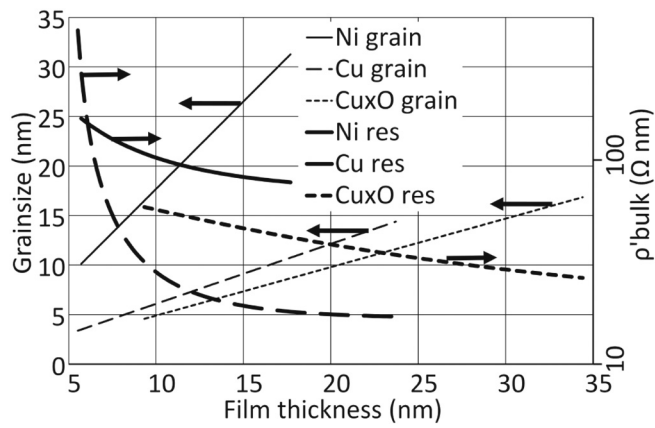


Fig. 4. Comparison of ρ'_{bulk} and grain size for Ni and Cu UTMFs and Cu_xO TFs against film thickness. Arrows point to the vertical axis used for each plot.

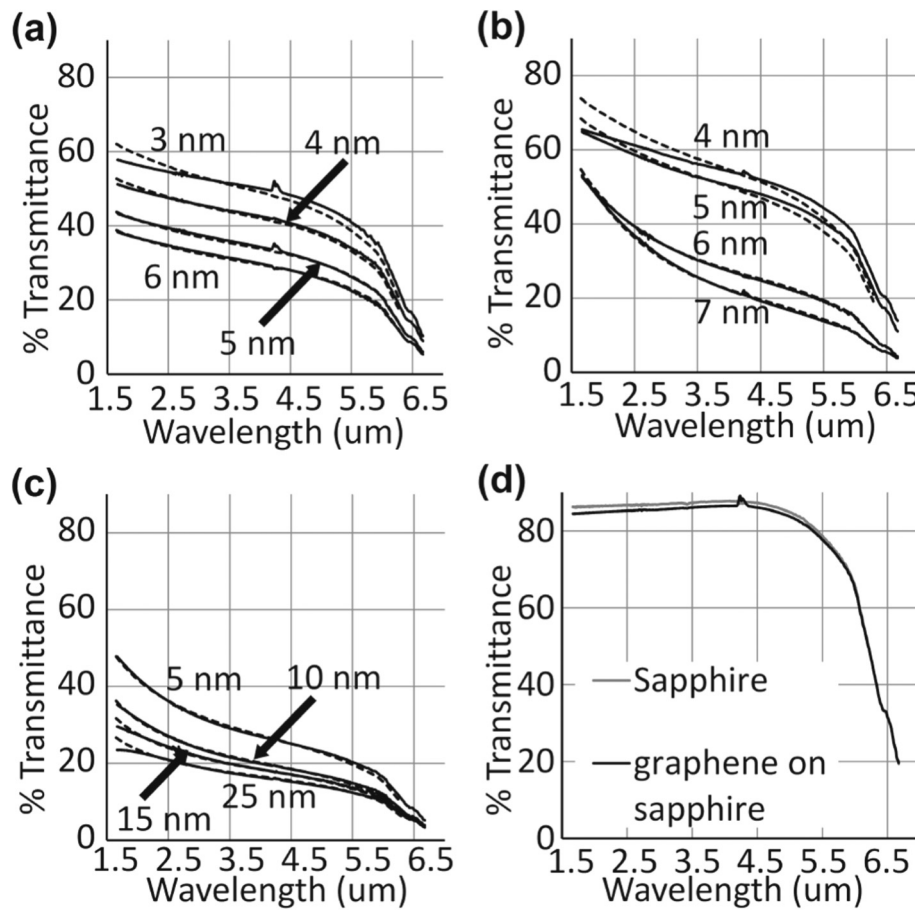


Fig. 5. Transmittance (%) vs. λ (μm) for selected values of t_{est} (nm) for sapphire substrate with (a) Ni and (b) Cu UTMFs, (c) Cu_xO TFs and (d) CVD graphene monolayer. Note that in (a)–(c) solid lines represent experimental data while dashed lines represent modelled data.

values of λ for small, comparable values of t_{est} . Cu_xO TFs are observed to have a transmittance comparable to Ni UTMFs for similar t_{est} values and small wavelengths, with the performance for Cu_xO TFs being poorer at larger wavelengths.

A model was adopted to explain the data collected based on the Maxwell-Garnett formula [33]:

$$\frac{\epsilon(\omega) - \epsilon_i(\omega)}{\epsilon(\omega) + 2\epsilon_i(\omega)} = (1-x) \frac{\epsilon_m(\omega) - \epsilon_i(\omega)}{\epsilon_m(\omega) + 2\epsilon_i(\omega)} \quad (6)$$

This describes the effective complex dielectric constant $\epsilon(\omega)$ of a mixed medium with metallic spherical particles having complex dielectric constant $\epsilon_m(\omega)$ in another insulating medium having complex dielectric constant $\epsilon_i(\omega)$. x gives the volume fraction of insulator. Furthermore, a shape factor L_m is introduced to account for the possibility of non-spherical particles:

$$\frac{\epsilon(\omega) - \epsilon_i(\omega)}{L_m \epsilon(\omega) + (1-L_m)\epsilon_i(\omega)} = (1-x) \frac{\epsilon_m(\omega) - \epsilon_i(\omega)}{L_m \epsilon_m(\omega) + (1-L_m)\epsilon_i(\omega)} \quad (7)$$

L_m takes a minimum value of 0 for flat discs in the plane of the thin film, a maximum value of 1 for flat discs perpendicular to the plane of the film and 1/3 for spherical particles. Values in between represent oblate spheroids with circular cross-section parallel ($0 < L_m < 1/3$) and perpendicular ($1/3 < L_m < 1$) to the film. Considering the large proportion of metal which we expect in our films, the model has to be modified to represent insulating particles within a metallic medium, which results in $\epsilon_i(\omega)$ and $\epsilon_m(\omega)$ to switch positions, $(1-x)$ to become x and L_m to become L_i , the shape factor for the insulating inclusions. A significant simplification occurs for wavelengths larger than the near-infrared ($\lambda > 1 \mu\text{m}$) since in this wavelength range $|\epsilon_m(\omega)| \gg |\epsilon_i(\omega)|$ so that the expression used reduces to [33]

$$\epsilon(\omega) = \epsilon_m(\omega) \left(\frac{(1-x)(1-L_i)}{1-L_i(1-x)} \right) \quad (8)$$

Note that this expression is not dependent on $\epsilon_i(\omega)$.

The values of $\epsilon_m(\omega)$ used in the above equation cannot however be those for the bulk material due to the granular structure previously discussed. $\epsilon_m(\omega)$ can be decomposed as

$$\epsilon_m(\omega) = \epsilon_m^f(\omega) + \epsilon_m^i(\omega) \quad (9)$$

where $\epsilon_m^f(\omega)$ is the free-electron, intra-band component of the dielectric constant, given by Drude, and $\epsilon_m^i(\omega)$ is the inter-band component of the dielectric constant. Bulk values of $\epsilon_m(\omega)$ were obtained from literature for Ni and Cu [34], and $\epsilon_m^f(\omega)$ was calculated based on the Brendel-Bormann model used in the same source. Thus $\epsilon_m^i(\omega)$, which we assumed to be unchanged in accordance with literature, could be extracted. The intra-band component is given by

$$\epsilon_m^f(\omega) = 1 - \frac{\tilde{\omega}_p^2 \tau}{\omega(\omega\tau + i)} \quad (10)$$

where $\tilde{\omega}_p$ is the free electron plasma frequency, which we kept unchanged from the bulk value, and τ is the conduction electron relaxation time. τ is known to decrease for highly granular films [33] and as such it was used as a fitting parameter by applying a factor τ_o from 0 to 1 such that $\tau_{film} = \tau_o \tau_{bulk}$.

Furthermore, the role of the oxide layer on top of the metal/void partition layer could now not be disregarded. Due to the highly granular structure of the film, the oxide/metal interface was disregarded, assuming that the transition from the oxide layer to the metal/void layer is gradual. Due to the grain structure it was also assumed that the oxide cover would not be complete nor uniform. As such a weighing

Table 4

Optical model constants of films having estimated thickness t_{est} ; insulating inclusion shape factor L_i , conduction electron relaxation time reduction factor τ_o and oxide/metal reflection weighing factor w .

	t_{est} (nm)	L_i	τ_o	w
Ni UTMFs	3	1.7/3	5×10^{-6}	1
	4	1.5/3	10×10^{-6}	1
	5	2.1/3	40×10^{-6}	0.75
	6	2.35/3	50×10^{-6}	0.60
Cu UTMFs	4	0.1/3	0.0065	1
	5	2.32/3	0.0065	1
	6	2.55/3	0.023	1
	7	2.7/3	0.04	0.95
Cu_xO TFs	5	2.2/3	0.01	0.55
	10	2.42/3	0.01	0.4
	15	2.6/3	0.01	0.4
	25	2.8/3	0.01	0.4

factor w was introduced such that when $w = 0$ the reflection at the film/air interface is purely dependent on the metal/void layer and when $w = 1$ it depends entirely on the oxide layer on top. Note that the film thicknesses t_m and the insulator volume fractions x used were those obtained by ellipsometry and given in Tables 1 and 3. Refractive index values for NiO, Cu_2O and sapphire were collected from various sources [35,36].

Table 4 collects the constants that were manually fit so as to be able to obtain the results seen in Fig. 5. Comparing these results with the ones in Table 1 for ellipsometry it is observed that variations in w largely follow what is expected as there is a decrease of the oxide effect on reflection for thicker films, with the biggest variation seen for Ni UTMFs. This is similar to what we see from the ellipsometry data. L_i is seen to increase for all samples, with most values larger than 1/3, suggesting that most insulator inclusions were perpendicular to the plane of the film. This is also justified by literature [20], where the MS-model hinges on the fact that inclusions tend to become more vertical in aspect ratio as the thickness of the film increases, thus assumptions required by the model regarding the vertical nature of grain boundaries can be made with confidence. Values of τ_o for Cu UTMFs and Cu_xO TFs were found to be typically more than 2 orders of magnitude larger than for Ni UTMFs. Increase of τ_o with increased metal proportion is expected [33] and indeed observed for Cu UTMFs and Ni UTMFs but not for Cu_xO TFs, where it was constant.

Fig. 6 illustrates the relationship between the key optical property and key electrical property for TC use in LC-SLMs. For mono-layer to quad-layer CVD graphene the transmittance data was collected at 550 nm for samples on polyethylene-naphthalate (PEN). Due to the

similarity of the results obtained to that collected for 2.3 μm for monolayer graphene a direct comparison is made in Fig. 6 by multiplying the transmittance for graphene extracted from the on PEN samples with the empirical result we obtained for bare sapphire samples at 2.3 μm ; T = 86.6%. Cu_xO TFs have the poorest performance. Having a larger fraction of oxygen sputter flow rate produces more transmissive films, but the resistance would also increase. Optimising this trade-off is a non-trivial challenge in its own right, and depends largely on the R_\square constraints of the device to be developed. Cu_xO TFs are therefore henceforth disregarded in this work. Ni UTMFs are seen to perform better than Cu UTMFs for R_\square up to $\approx 500 \Omega/\square$, while Cu UTMFs take over at larger values of R_\square , corresponding to thinner films. Graphene performs considerably better than all the other materials tested, with mono-layer on sapphire samples having transmittance of 85.1% for $\lambda = 2.3 \mu m$ and a sheet resistance of $360 \pm 34 \Omega/\square$. Manipulated on PEN results suggest that multi-layer graphene can be used if smaller R_\square values are required, which is particularly useful for applications where the electrode geometry makes voltage drop along the electrode a primary concern. This since adding more layers results in only a marginally smaller transmittance: For quad-layer samples the transmittance is 78%, which is still better than that of all other films tested irrespective of their R_\square value.

3.4. Stability under further processing

Moving from a TC coated substrate to a final product involves a number of process steps, with the alignment layer coating and baking being the most pivotal since the polyimide layer is directly in contact with the TC and the required imidisation bake is the highest temperature to which the TC is subjected to 200 °C for 120 min [37] according to our standard lab procedures. Degradation due to ageing is also a concern both for obtaining repeatable information at the experimental stage but also out in the field for finalised products.

Oxidation in air is the primary concern regarding stability at the pre-assembly stage for Ni and Cu UTMFs. Fig. 7 shows the increase in R_\square due to oxidation for Ni and Cu UTMFs of various t_{est} values under both the effect of ageing and of baking at different temperatures. It can be seen that Ni UTMFs oxidise at a much slower rate than Cu, with change in R_\square for Ni UTMFs being minimal over a 156 h ageing period, while R_\square for Cu UTMFs increased three-fold in the same period of time. Baking at 160 °C for 120 min approximately doubles the R_\square value of Ni UTMFs for both 3 nm and 6 nm films but for 6 nm Cu UTMFs R_\square increases to $> 9 M\Omega/\square$ in 5 min for a 120 °C bake and in 30 min for a 100 °C bake. These results largely agree with similar findings in literature [16,17]. Such increase in R_\square value was also observed during the imidisation bake, and as such the covering of the TC by the polyimide precursor did not slow the oxidation process enough to make Cu UTMFs viable. Baking in an atmosphere without oxygen could be a solution pending data on the post-bake oxidation rate of UTMFs when covered with a polyimide layer.

Graphene is thermally stable in air in our temperature range [38], as confirmed by Fig. 7a. However, contaminants like water, oxygen and carbon dioxide act as dopants, reducing the sheet resistance of the CVD graphene [39]. These dopants can be removed by annealing as we can see in Fig. 7b. Another advantage of graphene over UTMFs is that metallic films are known to cause degradation of the LC-layer and lowering of the breakdown voltage of devices as ions from the film diffuse into the LC-layer. This is mitigated by driving the device using alternating currents. Graphene does not have this drawback at all, potentially adding to the lifetime of the system [28,40].

3.5. Lithographic potential

The ability to pattern TC materials is vital in creating addressable structures able to set up the controllable phase profiles desired across the LC-device. Fig. 8 shows the AFM topography for an 80 $\mu m \times 80 \mu m$

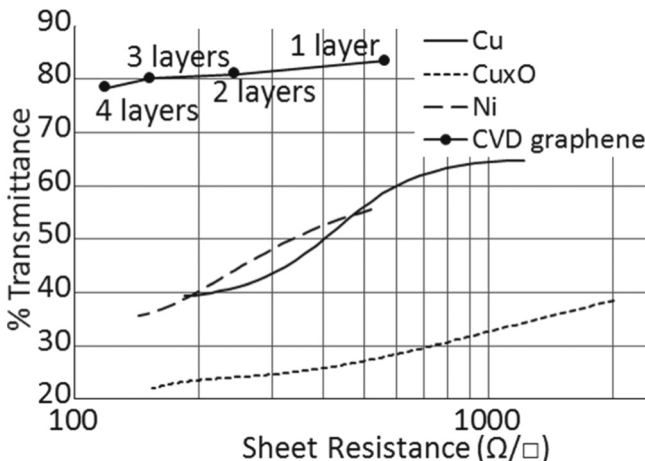


Fig. 6. Transmittance (%) on sapphire samples at $\lambda = 2.3 \mu m$ vs. $R_\square (\Omega/\square)$ for mono-layer to quad-layer CVD graphene, Ni and Cu UTMFs and Cu_xO TFs.

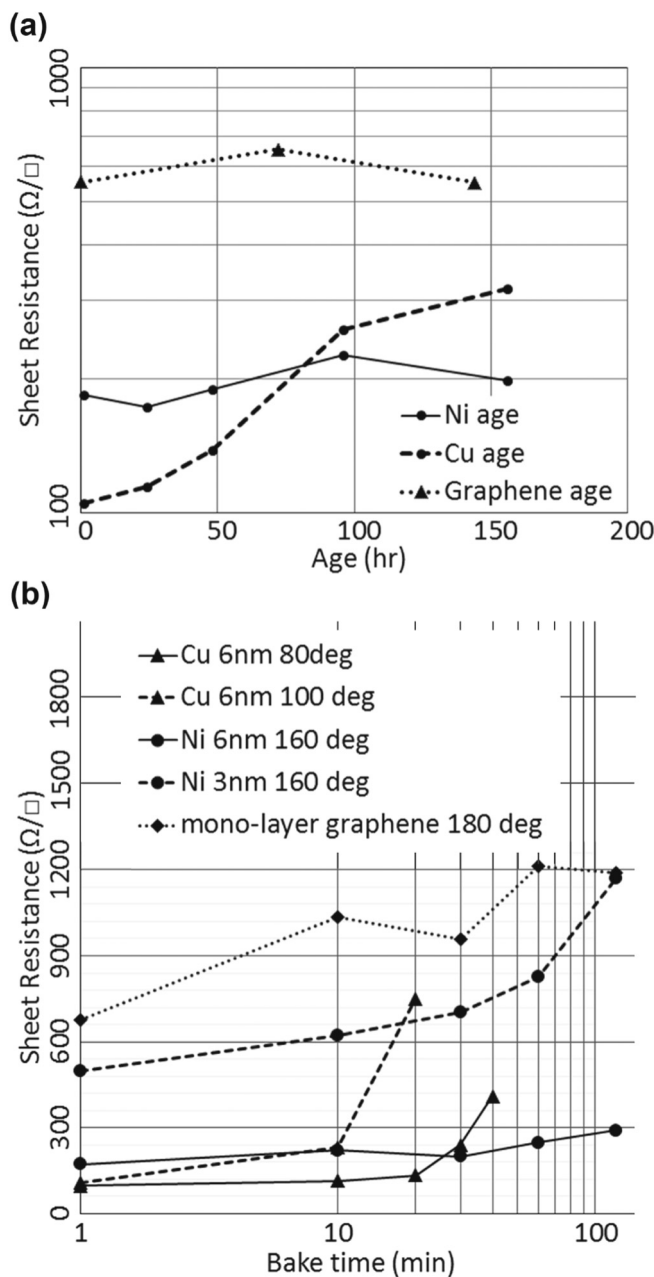


Fig. 7. R_{\square} (Ω/\square) vs. (a) age (h) and (b) bake time (min) respectively for mono-layer CVD graphene and Ni and Cu UTMFs.

area that has a repeating pattern made up of 3 μm wide, $t_{\text{est}} = 3 \text{ nm}$, Ni UTMF electrodes and 12 μm spacing on sapphire, along with a surface profile for the grating. Patterning was done by lift-off as described in Section 2.

In Fig. 8b the surface profile height is seen to spike at the edges of the electrodes. In a lift-off process this occurs when the metallic film deposited is continuous, as seen in Fig. 9. When the resist is stripped this results in the spikes we observed [41]. Since a large electric field tends to occur at spikes these are undesirable in an LC-SLM as this requires an electric field to set up the corresponding phase profile. A solution is to use an undercut resist layer which ensures that the metallic film is not continuous [42].

Typical geometry measured from the profile for this grating is as follows: electrode height $7.3 \pm 0.3 \text{ nm}$, electrode width $2.76 \pm 0.02 \mu\text{m}$, electrode spacing $10.74 \pm 0.14 \mu\text{m}$, grating period $13.50 \pm 0.14 \mu\text{m}$ and spacing to electrode width ratio 0.257 ± 0.005 . The electrode

height measured is within a standard deviation of the t_m value found by ellipsometry in Table 1. This is a verification that the ellipsometric model applied is indeed appropriate. The electrode width and electrode spacing are both underestimated, but since the grating period is also underestimated this suggests that the mask itself might not have been entirely faithful to the design, or that the mask copying process from the master shrunk the design slightly. Irrespective of this, given that we have a spacing to electrode width ratio larger than 0.25, slight over-exposure or over-development might have occurred.

For the required resolution of a few microns graphene can be patterned by laser ablation [43], e-beam lithography [44] or photolithography [45]. Laser ablation and e-beam lithography are both slow and expensive compared to photolithography but can achieve sub-micron structures. Resist residue after stripping dopes the graphene and causes loss of carrier mobility and reduction in sheet resistance [46]. If required, this residue can be removed by various processes such as chemical cleaning using an ethyl-2-pyrrolidone based remover [45] or via an annealing bake in Ar for PMMA [47]. For e-beam lithography and photolithography graphene can be etched with oxygen plasma [44,48].

3.6. Electro-optic response

Developing LC-SLM devices requires knowledge of the electro-optic (EO) response for the LC material used given the thickness of the LC layer, its alignment and the TC used. Once this is established it is possible to obtain a function relating the voltage applied to each pixel with, for amplitude modulating devices, the radiation transmitted or, for phase modulating devices, the phase delay.

Fig. 10 gives the EO response at $\lambda = 2.3 \mu\text{m}$ for the single pixel cells assembled. Note that for each extremum in the curves we have a π phase shift and that the curves have a long tail with 0π phase shift attained for an infinite voltage applied [49]. For both Ni UTMF cells and mono-layer graphene cells a maximum phase delay (δ_{max}) of $\approx 3\pi$ can be attained. We expect this to be equal since it is a function of the LC layer thickness.

From Table 5 the transmittance of the mono-layer graphene cell is more than four times better than that of the $t_{\text{est}} = 6 \text{ nm}$ Ni UTMF cell. A $t_{\text{est}} = 3 \text{ nm}$ Ni UTMF cell would have yielded better transmittance results and assembly of such a cell was attempted but the alignment layer precursor was found to destroy the TC samples, likely due to the formic acid. Preliminary tests conducted suggest that an alignment precursor which contains solvents such as NMP instead of acids would enable assembly of cells with thinner Ni UTMFs. Note that any alignment coating attempted on mono-layer graphene also resulted in a damaged layer and therefore alignment rubbing was done directly on the mono-layer graphene for the working cells. The contrast ratio (CR) between driven light and dark states was also better for the graphene cell than for the Ni UTMF cell, even though there was no dedicated alignment layer in the former.

Comparing the transmittance data for TC on sapphire samples in Fig. 5 to transmittance data for the assembled cells on sapphire in Fig. 10 we have a 3.4% and a 17.4% drop in transmittance, for Ni UTMF and mono-layer graphene TCs respectively, between TC on sapphire samples and assembled cell samples. For Ni UTMFs this is a 49.0% drop, which indicates that the absorption of the LC BL037 is negligible at $\lambda = 2.3 \mu\text{m}$ for the thicknesses typically used in LC SLMs. For mono-layer graphene the drop is 4.0%, suggesting that there is a high degree of refractive index matching between the sapphire, graphene and LC.

In Fig. 10 it can be observed that the EO curve for the graphene cell is shifted towards larger voltages compared to the Ni UTMF cell. This suggests either an increased contact resistance between the connecting wires and the TCs or else an increased voltage drop along the TC electrode itself, which is dependent on the R_{\square} value of the TC.

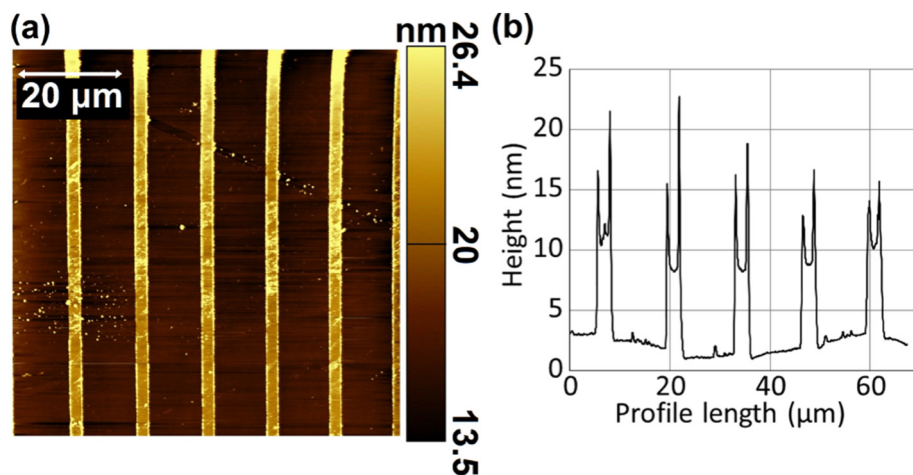


Fig. 8. (a) AFM $80\mu\text{m} \times 80\mu\text{m}$ topography image and (b) surface profile for grating made up of $3\mu\text{m}$ wide Ni UTMF of $t_{\text{est}} = 3\text{ nm}$ electrode and $12\mu\text{m}$ spacing on sapphire.

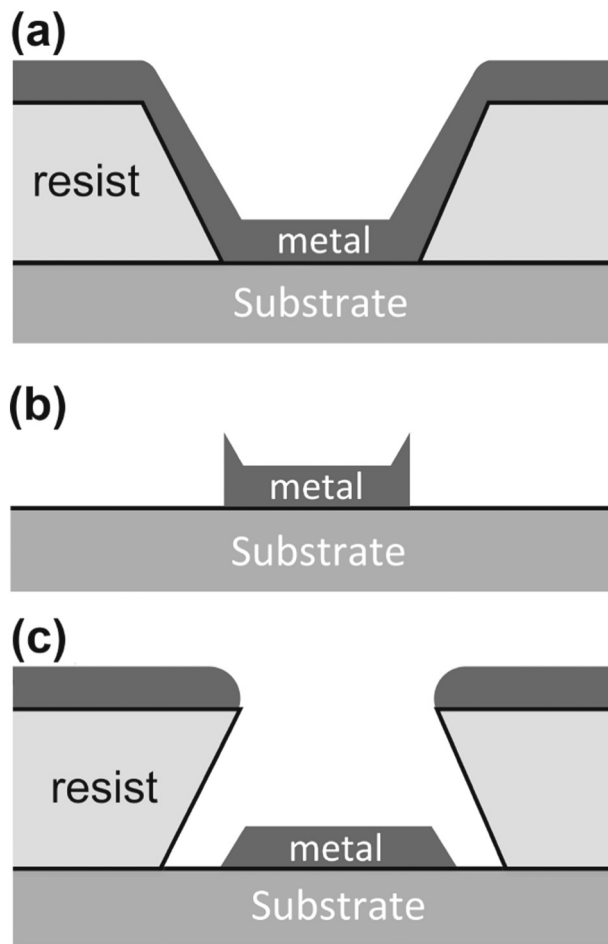


Fig. 9. Lift-off for a tapered resist layer (a) before and (b) after stripping, showing formation of spikes at the edges of the electrode. Lift-off for an (c) undercut resist layer with spikes absent.

4. Conclusions

Ni UTMFs and CVD mono-layer graphene were found to be suitable Mid-IR transparent conductors, applicable at least in the context of further Mid-IR LC-SLM proof-of-concept work. This given a 65% down to 56% and > 97% transmittance respectively, when substrate contribution is subtracted, for the application-interesting Mid-IR range of

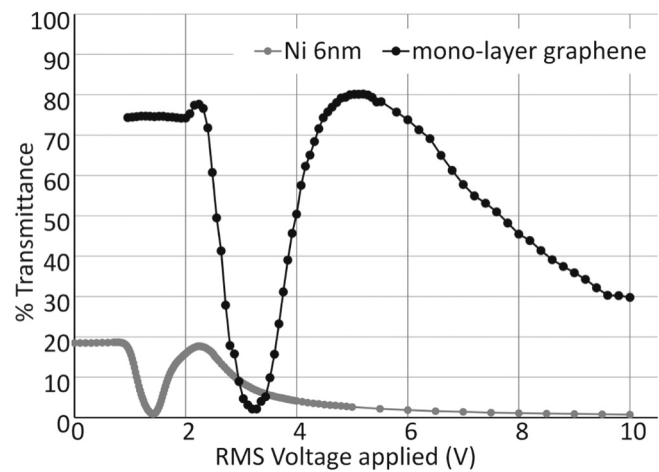


Fig. 10. Transmittance (%) at $\lambda = 2.3\mu\text{m}$ vs. applied root mean square (RMS) voltage (V), or electro-optic (EO) response, for BL037 filled, anti-parallel aligned, $15\mu\text{m}$ thick LC cells having $t_{\text{est}} = 6\text{ nm}$ Ni UTMF or mono-layer graphene electrodes on sapphire respectively.

Table 5

Results extracted from EO response curves in Fig. 10 comparing Ni UTMF and graphene cells. δ_{max} is the maximum phase delay, T (%) is the transmittance percentage and CR is the contrast ratio between minima and maxima in the curve.

TC	$t_{\text{est}} = 6\text{ nm}$ Ni UTMF	Mono-layer graphene
δ_{max}	$\approx 3\pi$	$\approx 3\pi$
T (%)	18.7	81.1
CR	25.0	50.7

$\lambda = 2.3\mu\text{m}$ to $4.5\mu\text{m}$ and R_{\square} values of $747 \pm 86\Omega/\square$ and $360 \pm 34\Omega/\square$ respectively. Both handled further processing well, Nickel was patterned successfully and literature shows this is also possible for graphene. Transmissive LC cells were assembled for both Ni UTMFs and mono-layer graphene TCs on sapphire, with the former having T = 18.7% and CR = 25.0, and the latter having T = 81.1% and CR = 50.7.

Conflict of interest

There are no conflicts to declare.

Acknowledgments

The authors thank Ms. Kasia Surowiecka for her technical help. This work was supported by the Defence Science and Technology Laboratory through an industrial CASE studentship with EPSRC. We also acknowledge funding from the ERC grant Hetero2D, the Graphene Flagship (grant No. 696656), the EPSRC grant EP/P02534X/1, the Trinity College, University of Cambridge and the Isaac Newton Trust.

References

- [1] M. Schadt, Liquid crystal materials and liquid crystal displays, *Annu. Rev. Mater. Sci.* 27 (1997) 305–379, <http://dx.doi.org/10.1146/annurev.matsci.27.1.305>.
- [2] S. Serati, J. Stockley, Advances in liquid crystal based devices for wavefront control and beamsteering, in: M.T. Gruneisen, J.D. Gonglewski, M.K. Giles (Eds.), *Advanced Wavefront Control: Methods, Devices, and Applications III*, vol. 5894, 2005, <http://dx.doi.org/10.1117/12.623191>.
- [3] F. Peng, Y. Chen, S.-T. Wu, S. Tripathi, R. Twieg, Low loss liquid crystals for infrared applications, *Liq. Cryst.* 41 (11) (2014) 1545–1552, <http://dx.doi.org/10.1080/02678292.2014.932452>.
- [4] I.C. Khoo, Nonlinear optics of liquid crystalline materials, *Phys. Rep.* 471 (5–6) (2009) 221–267, <http://dx.doi.org/10.1016/j.physrep.2009.01.001>.
- [5] T.K. Ewing, W.R. Folks, Liquid crystal on silicon infrared scene projectors, *Technol. Synth. Environ. Hardware-in-the-Loop Test. X* 5785 (1) (2005) 36–45, <http://dx.doi.org/10.1117/12.606462>.
- [6] C.M. Titus, J. Pouch, H.D. Nguyen, F. Miranda, P.J. Bos, Diffraction efficiency of thin film holographic beam steering devices, in: J.D. Gonglewski, M.A. Vorontsov, M.T. Gruneisen, S.R. Restaino, R.K. Tyson (Eds.), *High-Resolution Wavefront Control: Methods, Devices, and Applications IV*, vol. 4825, 2002, <http://dx.doi.org/10.1117/12.453891>.
- [7] A.R. Downs, A035059-A Review of Atmospheric Transmission Information in the Optical and Microwave Spectral Regions, (1976) <http://www.dtic.mil/dtic/tr/fulltext/u2/a035059.pdf> (accessed 06.11.17).
- [8] G. Overton, Photonics Applied: Defense: IR Countermeasures Aim for Safer Flights, (2011) <http://www.laserfocusworld.com/articles/print/volume-47/issue-8/features/photonics-applied-defense-ir-countermeasures-aim-for-safer-flights.html> Laser Focus World. 8 (accessed 06.11.17).
- [9] M. Song, E. Park, M. Seop Hyun, T. Hyun Kim, H. Yeoun Kim, G. Lee, Studies on transmittance of silicon with AR coating films for IR transparent window, in: P.D. LeVan, A.K. Sood, P.S. Wijewarnasuriya, A.I. D'Souza (Eds.), *Infrared Sensors, Devices, and Applications II*, vol. 8512, 2012, <http://dx.doi.org/10.1117/12.928346>.
- [10] J. Hecht, Photonic Frontiers: DARPA Projects: DARPA's Photonics Projects - At the Edge of Possibility, (2011) <http://www.laserfocusworld.com/articles/print/volume-47/issue-9/features/photonics-frontiers-darpa-projects-darpas-photonics-projects-at-the-edge-of-possibility.html> Laser Focus World. 9 (accessed 06.11.17).
- [11] R. Miller, G. Mooty, J.M. Hilkert, Gimbal system configurations and line-of-sight control technologies for small UAV applications, in: D.J. Henry, D.A. Lange, D.L. von Berg, S.D. Rajan, T.J. Walls, D.L. Young (Eds.), *Airborne Intelligence, Surveillance, Reconnaissance (ISR) Systems and Applications X*, vol. 8713, 2013, <http://dx.doi.org/10.1117/12.2015777>.
- [12] P.F. McManamon, T.A. Dorschner, D. Corkum, L. Friedman, D. Hobbs, M. Holz, S. Liberman, H. Nguyen, D. Resler, R. Sharp, Watson, Optical phased array technology, *Proc. IEEE* 84 (2) (1996) 268–298, <http://dx.doi.org/10.1109/5.482231>.
- [13] X. Wang, B. Wang, J. Pouch, F. Miranda, J.E. Anderson, P.J. Bos, Performance evaluation of a liquid-crystal-on-silicon spatial light modulator, *Opt. Eng.* 43 (2004) 2769–2774, <http://dx.doi.org/10.1117/1.1794706>.
- [14] S.M. Kelly, M.O. Neill, Handb. Adv. Electron. Photonic Mater. Devices, Vol. 7 Liq. Crystals, Disp. Laser Mater. vol. 7, (2000), <http://dx.doi.org/10.1016/b978-012513745-4/50057-3>.
- [15] X. Zhu, W. Sun, F. Tao, X. Cao, X. Zhang, Infrared transmission characteristic of indium-tin-oxide thin films prepared by femtosecond pulsed laser deposition, in: H. Gong, Z. Shi, Q. Chen, J. Lu (Eds.), *International Symposium on Photoelectronic Detection and Imaging 2013: Infrared Imaging and Applications*, vol. 8907, 2013, <http://dx.doi.org/10.1117/12.2033172>.
- [16] M.R. Pinnel, Oxidation of nickel and nickel-gold alloys in air at 50–150 °C, *J. Electrochem. Soc.* 126 (7) (1979) 1274–1281, <http://dx.doi.org/10.1149/1.2129256>.
- [17] S.-K. Lee, H.-C. Hsu, W.-H. Tuan, Oxidation behavior of copper at a temperature below 300 C and the methodology for passivation, *Mater. Res.* 19 (1) (2016) 51–56, <http://dx.doi.org/10.1590/1980-5373-MR-2015-0139>.
- [18] R. Pal, On the electrical conductivity of particulate composites, *J. Compos. Mater.* 41 (20) (2007) 2499–2511, <http://dx.doi.org/10.1177/0021998307076489>.
- [19] H.C. Lu, C.L. Chu, C.Y. Lai, Y.H. Wang, Property variations of direct-current reactive magnetron sputtered copper oxide thin films deposited at different oxygen partial pressures, *Thin Solid Films* 517 (2009) 4408–4412, <http://dx.doi.org/10.1143/JJAP.37.1945>.
- [20] A.F. Mayadas, M. Shatzkes, Electrical-resistivity model for polycrystalline films: the case of arbitrary reflection at external surfaces, *Phys. Rev. B* 1 (4) (1970) 1382–1389, <http://dx.doi.org/10.1103/PhysRevB.1.1382>.
- [21] A.S. Reddy, H.H. Park, V.S. Reddy, K.V.S. Reddy, N.S. Sarma, S. Kaleemulla, S. Uthanna, P.S. Reddy, Effect of sputtering power on the physical properties of dc magnetron sputtered copper oxide thin films, *Mater. Chem. Phys.* 110 (2–3) (2008) 397–401, <http://dx.doi.org/10.1016/j.matchemphys.2008.02.031>.
- [22] P. Klapetek, D. Necas, C. Anderson, *Gwyddion User Guide*, (2009) <http://www.gwyddion.net/download/user-guide/gwyddion-user-guide-en.pdf> (accessed 06.11.17).
- [23] J.M. Camacho, A.I. Oliva, Surface and grain boundary contributions in the electrical resistivity of metallic nanofilms, *Thin Solid Films* 515 (4) (2006) 1881–1885, <http://dx.doi.org/10.1016/j.tsf.2006.07.024>.
- [24] M.R. Querry, Optical Constants, Defence Technical Information Centre, (1985) <http://www.dtic.mil/docs/citations/ADA158623> (accessed 06.11.17).
- [25] K. Miedzinska, B. Hollebone, J. Cook, Optical properties and assignment of the absorption spectra of sputtered mixed valence nickel oxide films, *J. Phys. Chem. Solids* 49 (11) (1988) 1355–1362, [http://dx.doi.org/10.1016/0022-3697\(88\)90219-3](http://dx.doi.org/10.1016/0022-3697(88)90219-3).
- [26] K.S. Novoselov, A.K. Geim, S.V. Morozov, D. Jiang, Y. Zhang, S.V. Dubonos, I.V. Grigorieva, A.A. Firsov, Electric field effect in atomically thin carbon films, *Science* 306 (5696) (2004) 666–669, <http://dx.doi.org/10.1126/science.1102896>.
- [27] W. Wu, Q. Yu, P. Peng, Z. Liu, J. Bao, S.-S. Pei, Control of thickness uniformity and grain size in graphene films for transparent conductive electrodes, *Nanotechnology* 23 (3) (2012) 035603, <http://dx.doi.org/10.1088/0957-4484/23/3/035603>.
- [28] P. Blake, P.D. Brimicombe, R.R. Nair, T.J. Booth, D. Jiang, F. Schedin, L.A. Ponomarenko, S.V. Morozov, H.F. Gleeson, E.W. Hill, A.K. Geim, K.S. Novoselov, Graphene-based liquid crystal device, *Nano Lett.* 8 (6) (2008) 1704–1708, <http://dx.doi.org/10.1021/nl0806491>.
- [29] D. Gall, Electron mean free path in elemental metals, *J. Appl. Phys.* 119 (8) (2016) 085101, <http://dx.doi.org/10.1063/1.4942216>.
- [30] M. Angadi, L. Udashan, Electrical properties of thin nickel films, *Thin Solid Films* 79 (2) (1981) 149–153, [http://dx.doi.org/10.1016/0040-6090\(81\)90272-8](http://dx.doi.org/10.1016/0040-6090(81)90272-8).
- [31] G. Brandli, J. Olsen, Size effects in electron transport in metals, *Mater. Sci. Eng.* 4 (2) (1969) 61–83, [http://dx.doi.org/10.1016/0025-5416\(69\)90046-9](http://dx.doi.org/10.1016/0025-5416(69)90046-9).
- [32] V. Timoshhevskii, Y. Ke, H. Guo, D. Gall, The influence of surface roughness on electrical conductance of thin Cu films: an ab initio study, *J. Appl. Phys.* 103 (11) (2008) 9–12, <http://dx.doi.org/10.1063/1.2937188>.
- [33] R. Cohen, G. Cody, M. Coutts, B. Abeles, Optical properties of granular silver and gold films, *Phys. Rev. B* 8 (8) (1973) 3689–3701, <http://dx.doi.org/10.1103/PhysRevB.3689>.
- [34] A.D. Rakic, A.B. Djurisic, J.M. Elazar, M.L. Majewski, Optical properties of metallic films for vertical-cavity optoelectronic devices, *Appl. Opt.* 37 (22) (1998) 5271–5283, <http://dx.doi.org/10.1364/ao.37.005271>.
- [35] R.D. Shannon, R.C. Shannon, O. Medenbach, R.X. Fischer, Refractive index and dispersion of fluorides and oxides, *J. Phys. Chem. Ref. Data* 31 (4) (2002) 931–970, <http://dx.doi.org/10.1063/1.1497384>.
- [36] M. Weber, *Handbook of Optical Materials, Laser & Optical Science & Technology*, Taylor & Francis, 2002.
- [37] Y. LIANG, Liquid Crystal Alignment Agent, and Liquid Crystal Alignment Film and Liquid Crystal Display Element Formed From the Liquid Crystal Alignment Agent. US Patent App. 13/467,811, (2012).
- [38] H.Y. Nan, Z.H. Ni, J. Wang, Z. Zafar, Z.X. Shi, Y.Y. Wang, The thermal stability of graphene in air investigated by Raman spectroscopy, *J. Raman Spectrosc.* 44 (7) (2013) 1018–1021, <http://dx.doi.org/10.1002/jrs.4312>.
- [39] G.V. Bianco, M. Losurdo, M.M. Giangregorio, P. Capezzuto, G. Bruno, Exploring and rationalising effective n-doping of large area CVD-graphene by NH₃, *Phys. Chem. Chem. Phys.* 16 (2014) 3632–3639, <http://dx.doi.org/10.1039/C3CP54451F>.
- [40] Y. Wu, X. Ruan, C.-H. Chen, Y.J. Shin, Y. Lee, J. Niu, J. Liu, Y. Chen, K.-L. Yang, X. Zhang, J.-H. Ahn, H. Yang, Graphene/liquid crystal based terahertz phase shifters, *Opt. Express* 21 (18) (2013) 21395–21402, <http://dx.doi.org/10.1364/OE.21.021395>.
- [41] M. Dimaki, M. Vergani, A. Heiskanen, D. Kwasny, L. Sasso, M. Carminati, J.A. Gerrard, J. Emneus, W.E. Svendsen, A compact microelectrode array chip with multiple measuring sites for electrochemical applications, *Sensors* 14 (6) (2014) 9505–9521, <http://dx.doi.org/10.3390/s140609505>.
- [42] H.S. Lee, J.-B. Yoon, A simple and effective lift-off with positive photoresist, *J. Micromech. Microeng.* 15 (11) (2005) 2136–2140, <http://dx.doi.org/10.1088/0960-1317/15/11/020>.
- [43] R. Sahin, E. Simsek, S. Akturk, Nanoscale patterning of graphene through femtosecond laser ablation, *Appl. Phys. Lett.* 104 (5) (2014) 053118, <http://dx.doi.org/10.1063/1.4864616>.
- [44] L. Liu, S. Tian, Y. Long, W. Li, H. Yang, J. Li, C. Gu, Tunable periodic graphene antidot lattices fabricated by e-beam lithography and oxygen ion etching, *Vacuum* 105 (Supplement C) (2014) 21–25, <http://dx.doi.org/10.1016/j.vacuum.2014.01.015>.
- [45] R. Shi, H. Xu, B. Chen, Z. Zhang, L.-M. Peng, Scalable fabrication of graphene devices through photolithography, *Appl. Phys. Lett.* 102 (11) (2013) 113102, <http://dx.doi.org/10.1063/1.4795332>.
- [46] K. Kim, A. Reina, Y. Shi, H. Park, L.-J. Li, Y. Lee, J. Kong, Enhancing the conductivity of transparent graphene films via doping, *Nanotechnology* 21 (28) (2010) 285205, <http://dx.doi.org/10.1088/0957-4484/21/28/285205>.
- [47] J. Fan, J. Michalik, L. Casado, S. Roddar, M. Ibarra, J. De Teresa, Investigation of the influence on graphene by using electron-beam and photo-lithography, *Solid State Commun.* 151 (21) (2011) 1574–1578, <http://dx.doi.org/10.1016/j.ssc.2011.07.028>.
- [48] H. Al-Mumen, F. Rao, W. Li, L. Dong, Singular sheet etching of graphene with oxygen plasma, *Nano-Micro Lett.* 6 (2) (2014) 116–124, <http://dx.doi.org/10.1007/BF03353775>.
- [49] L. Teng, M. Pivnenko, B. Robertson, R. Zhang, D. Chu, A compensation method for the full phase retardance nonuniformity in phase-only liquid crystal on silicon spatial light modulators, *Opt. Express* 22 (21) (2014) 26392–26402, <http://dx.doi.org/10.1364/OE.22.026392>.